2

Direct Reconstruction Methods in Ultrasound Imaging of Small Anomalies

Habib Ammari[1], Josselin Garnier*[,2], Vincent Jugnon[1], and Hyeonbae Kang[3]

[1] Department of Mathematics and Applications, Ecole Normale Supérieure, 45 Rue d'Ulm, 75005 Paris, France habib.ammari@ens.fr, vincent.jugnon@ens.fr
[2] Laboratoire de Probabilités et Modèles Aléatoires & Laboratoire Jacques-Louis Lions, Université Paris VII, Site Chevaleret, 75205 Paris Cedex 13, France garnier@math.jussieu.fr
[3] Department of Mathematics, Inha University, Incheon 402-751, Korea hbkang@inha.ac.kr

Summary. The aim of this chapter is to review direct (non-iterative) anomaly detection algorithms that take advantage of the smallness of the ultrasound anomalies. In particular, we numerically investigate their stability with respect to medium and measurement noises as well as their resolution.

2.1 Introduction

Ultrasound imaging is a noninvasive, easily portable, and relatively inexpensive diagnostic modality which finds extensive use in the clinic. The major clinical applications of ultrasound include many aspects of obstetrics and gynecology involving the assessment of fetal health, intra-abdominal imaging of the liver, kidney, and the detection of compromised blood flow in veins and arteries.

Operating typically at frequencies between 1 and 10 MHz, ultrasound imaging produces images via the backscattering of mechanical energy from interfaces between tissues and small structures within tissue. It has high spatial resolution, particularly at high frequencies, and involves no ionizing radiation. The weaknesses of the technique include the relatively poor soft-tissue contrast and the fact that gas and bone impede the passage of ultrasound waves, meaning that certain organs can not easily be imaged.

In this chapter, we review recent developments in the mathematical and numerical modelling of ultrasound anomaly detection at a fixed or multiple frequencies [1,3,6,7,9,11,12,20]. We construct different direct (non-iterative) anomaly detection algorithms that take advantage of the smallness of the ultrasound anomalies. In particular, MUltiple Signal Classification algorithm

H. Ammari (ed.), *Mathematical Modeling in Biomedical Imaging II*, Lecture Notes in Mathematics 2035, DOI 10.1007/978-3-642-22990-9_2,

(MUSIC), backpropagation, Kirchhoff migration, and topological derivative are investigated. Direct algorithms provide quite robust and accurate reconstruction of the location and of some geometric features of the anomalies, even with moderately noisy data. We numerically illustrate their stability with respect to medium and measurement noises as well as their resolution.

We also investigate multifrequency imaging. We illustrate that in the presence of (independent and identically distributed) measurement noises summing over frequencies a given imaging functional yields an improvement in the signal-to-noise ratio. However, if some correlation between frequency-dependent measurements exists, for example because of a medium noise, then summing over frequencies an imaging functional may not be appropriate. A single-frequency imaging functional at the frequency which maximizes the signal-to-noise ratio may give a better reconstruction.

When the acoustic medium is randomly heterogeneous, travel times cannot be known with accuracy so that images obtained with reverse time migration are noisy and not statistically stable, that is, they change with the realization of the random medium. Coherent Interferometry (CINT) has been shown to achieve a good compromise between resolution and deblurring for imaging in noisy environments from multiple frequency measurements [13, 14]. CINT consists of backpropagating the cross correlations of the recorded signals over appropriate space-time or space-frequency windows rather than the signals themselves. We provide a CINT strategy in ultrasound imaging.

The chapter is organized as follows. In Sect. 2.2 we formulate a model problem and recall an asymptotic expansion of the boundary pressure perturbations due to small acoustic anomalies. In Sect. 2.3 we review direct imaging algorithms from measurements at fixed or multiple frequencies based on the asymptotic expansion. In Sect. 2.4 we perform a variety of numerical tests to compare the performance of the developed direct imaging algorithms in terms of resolution and stability with respect to measurement and medium noises.

2.2 Problem Formulation

Consider an acoustic anomaly with constant bulk modulus K and volumetric mass density ρ. The background medium $\Omega \subset \mathbb{R}^d$ is smooth and homogeneous with bulk modulus and density equal to one. Suppose that the operating frequency ω is such that ω^2 is not an eigenvalue for the operator $-\Delta$ in $L^2(\Omega)$ with homogeneous Neumann boundary conditions. The scalar acoustic pressure u generated by the Neumann data g in the presence of the anomaly D is the solution to the Helmholtz equation:

$$\begin{cases} \nabla \cdot \Big(\mathbf{1}_{\Omega\setminus\overline{D}}(\boldsymbol{x}) + \rho^{-1}\mathbf{1}_D(\boldsymbol{x})\Big)\nabla u + \omega^2\big(\mathbf{1}_{\Omega\setminus\overline{D}}(\boldsymbol{x}) + K^{-1}\mathbf{1}_D(\boldsymbol{x})\big)u = 0 \ \text{ in } \Omega, \\ \dfrac{\partial u}{\partial \nu} = g \ \text{ on } \partial\Omega, \end{cases} \tag{2.1}$$

while the background solution U satisfies

$$\begin{cases} \Delta U + \omega^2 U = 0 \ \text{ in } \Omega, \\ \dfrac{\partial U}{\partial \nu} = g \ \text{ on } \partial\Omega. \end{cases} \tag{2.2}$$

Here, $\boldsymbol{\nu}$ is the outward normal to $\partial\Omega$ and $\mathbf{1}_D$ is the characteristic function of D.

The problem under consideration is the following one: given the field u measured at the surface of the domain Ω, we want to estimate the location of the anomaly D.

Suppose that the anomaly is $D = \boldsymbol{z}_a + \delta B$, where $\boldsymbol{z}_a$ is the "center" of D, B is a smooth reference domain which contains the origin, and δ, the characteristic size of D, is a small parameter.

We provide an asymptotic expansion of the boundary pressure perturbations, $u - U$, as δ goes to zero. For doing so, we need to introduce a few auxiliary functions that can be computed either analytically or numerically.

For B a smooth bounded domain in $\mathbb{R}^d$ and $0 < k \neq 1 < +\infty$ a material parameter, let $\hat{\boldsymbol{v}} = \hat{\boldsymbol{v}}(k, B)$ be the solution to

$$\begin{cases} \Delta \hat{\boldsymbol{v}} = \mathbf{0} \quad \text{in } \mathbb{R}^d \setminus \overline{B}, \\ \Delta \hat{\boldsymbol{v}} = \mathbf{0} \quad \text{in } B, \\ \hat{\boldsymbol{v}}|_- - \hat{\boldsymbol{v}}|_+ = \mathbf{0} \quad \text{on } \partial B, \\ k \dfrac{\partial \hat{\boldsymbol{v}}}{\partial \nu}\Big|_- - \dfrac{\partial \hat{\boldsymbol{v}}}{\partial \nu}\Big|_+ = \mathbf{0} \quad \text{on } \partial B, \\ \hat{\boldsymbol{v}}(\boldsymbol{\xi}) - \boldsymbol{\xi} \to \mathbf{0} \quad \text{as } |\boldsymbol{\xi}| \to +\infty. \end{cases} \tag{2.3}$$

Here we denote

$$v|_\pm(\boldsymbol{\xi}) := \lim_{t \to 0^+} v(\boldsymbol{\xi} \pm t\boldsymbol{\nu}_{\boldsymbol{\xi}}), \quad \boldsymbol{\xi} \in \partial B,$$

and

$$\frac{\partial v}{\partial \nu}\Big|_\pm (\boldsymbol{\xi}) := \lim_{t \to 0^+} \boldsymbol{\nu}_{\boldsymbol{\xi}}^T \nabla v(\boldsymbol{\xi} \pm t\boldsymbol{\nu}_{\boldsymbol{\xi}}), \quad \boldsymbol{\xi} \in \partial B,$$

if the limits exist, where $\boldsymbol{\nu}_{\boldsymbol{\xi}}$ is the outward unit normal to ∂B at $\boldsymbol{\xi}$ and T stands for the transpose (so that $\boldsymbol{a}^T\boldsymbol{b}$ is the scalar product of the two vectors $\boldsymbol{a}$ and $\boldsymbol{b}$). Recall that $\hat{\boldsymbol{v}}$ plays the role of the first-order corrector in the theory of homogenization [18].

Define the polarization tensor $\mathbf{M}(k, B) = (M_{pq})_{p,q=1}^d$ by

$$M_{pq}(k, B) := (k-1) \int_B \frac{\partial \hat{v}_q}{\partial \xi_p}(\boldsymbol{\xi})\, d\boldsymbol{\xi}, \tag{2.4}$$

where $\hat{\boldsymbol{v}} = (\hat{v}_1, \ldots, \hat{v}_d)^T$ is the solution to (2.3). The formula of the polarization tensor for ellipses will be useful. In dimension $d = 2$, let B be an

ellipse whose semi-axes are along the x_1- and x_2-axes and of length a and b, respectively. Then, $\mathbf{M}(k, B)$ takes the form [8]

$$\mathbf{M}(k, B) = (k-1)|B| \begin{pmatrix} \dfrac{a+b}{a+kb} & 0 \\ 0 & \dfrac{a+b}{b+ka} \end{pmatrix}. \tag{2.5}$$

For $\omega \geq 0$, let for $\boldsymbol{x} \neq 0$,

$$\Gamma_\omega(\boldsymbol{x}) = \begin{cases} \dfrac{e^{i\omega|\boldsymbol{x}|}}{4\pi|\boldsymbol{x}|}, & d = 3, \\ \dfrac{i}{4} H_0^{(1)}(\omega|\boldsymbol{x}|), & d = 2, \end{cases} \tag{2.6}$$

which is the outgoing fundamental solution for the Helmholtz operator $-(\Delta + \omega^2)$ in $\mathbb{R}^d$. Here, $H_0^{(1)}$ is the Hankel function of the first kind of order zero.

Let the integral operator $\mathcal{K}_\Omega^\omega$ be defined by

$$\mathcal{K}_\Omega^\omega[\varphi](\boldsymbol{x}) = \int_{\partial\Omega} \frac{\partial \Gamma_\omega(\boldsymbol{x}-\boldsymbol{y})}{\partial \nu(\boldsymbol{y})} \varphi(\boldsymbol{y}) d\sigma(\boldsymbol{y}), \quad \boldsymbol{x} \in \partial\Omega.$$

For $\boldsymbol{z} \in \Omega$, let us now introduce the Neumann function for $-(\Delta + \omega^2)$ in Ω corresponding to a Dirac mass at $\boldsymbol{z}$. That is, N_ω is the solution to

$$\begin{cases} -(\Delta_x + \omega^2) N_\omega(\boldsymbol{x}, \boldsymbol{z}) = \delta_{\boldsymbol{z}} & \text{in } \Omega, \\ \dfrac{\partial N_\omega}{\partial \nu} = 0 & \text{on } \partial\Omega. \end{cases} \tag{2.7}$$

We will need the following lemma from [10, Proposition 2.8].

Lemma 2.1 *The following identity relating the fundamental solution Γ_ω to the Neumann function N_ω holds:*

$$\left(-\frac{1}{2}\mathcal{I} + \mathcal{K}_\Omega^\omega \right)[N_\omega(\cdot, \boldsymbol{z})](\boldsymbol{x}) = \Gamma_\omega(\boldsymbol{x} - \boldsymbol{z}), \quad \boldsymbol{x} \in \partial\Omega, \ \boldsymbol{z} \in \Omega. \tag{2.8}$$

In (2.8), $\mathcal{I}$ denotes the identity.

Assuming that ω^2 is not an eigenvalue for the operator $-\Delta$ in $L^2(\Omega)$ with homogeneous Neumann boundary conditions, we can prove, using the theory of relatively compact operators, the existence and uniqueness of a solution to (2.1) at least for δ small enough [19]. Moreover, the following asymptotic formula for boundary pressure perturbations that are due to the presence of a small acoustic anomaly holds [7, 19].

Theorem 2.2 *Let u be the solution of (2.1) and let U be the background solution. Suppose that $D = \boldsymbol{z}_a + \delta B$, with $0 < (K, \rho) \neq (1, 1) < +\infty$. Suppose that $\omega\delta \ll 1$.*

(i) *For any* $\boldsymbol{x} \in \partial\Omega$,

$$u(\boldsymbol{x}) = U(\boldsymbol{x}) - \delta^d \Big(\nabla U(\boldsymbol{z}_a)^T \mathbf{M}(1/\rho, B) \nabla_{\boldsymbol{z}} N_\omega(\boldsymbol{x}, \boldsymbol{z}_a) + \omega^2 (K^{-1} - 1) |B| U(\boldsymbol{z}_a) N_\omega(\boldsymbol{x}, \boldsymbol{z}_a) \Big) + o(\delta^d), \tag{2.9}$$

where $\mathbf{M}(1/\rho, B)$ *is the polarization tensor associated with* B *and* $1/\rho$.

(ii) *Let* w *be a smooth function such that* $(\Delta + \omega^2) w = 0$ *in* Ω. *The weighted boundary measurements* $I_w[U, \omega]$ *defined by*

$$I_w[U, \omega] := \int_{\partial\Omega} (u - U)(\boldsymbol{x}) \frac{\partial w}{\partial \nu}(\boldsymbol{x}) \, d\sigma(\boldsymbol{x}) \tag{2.10}$$

satisfies

$$I_w[U, \omega] = -\delta^d \Big(\nabla U(\boldsymbol{z}_a)^T \mathbf{M}(1/\rho, B) \nabla w(\boldsymbol{z}_a) + \omega^2 (K^{-1} - 1) |B| U(\boldsymbol{z}_a) w(\boldsymbol{z}_a) \Big) + o(\delta^d). \tag{2.11}$$

The weighted boundary measurements $I_w[U, \omega]$ will be used for introducing MUSIC and backpropagation-type algorithms.

Suppose that the background domain contains P well-separated anomalies $D_p = \boldsymbol{z}_p + \delta B_p$, $p = 1, \ldots, P$, with volumetric mass density and bulk modulus denoted by ρ_p and K_p, respectively. Then, (2.9) yields

$$u(\boldsymbol{x}) = U(\boldsymbol{x}) - \delta^d \sum_{p=1}^{P} \Big(\nabla U(\boldsymbol{z}_p)^T \mathbf{M}(1/\rho_p, B_p) \nabla_{\boldsymbol{z}} N_\omega(\boldsymbol{x}, \boldsymbol{z}_p) + \omega^2 (K_p^{-1} - 1) |B_p| U(\boldsymbol{z}_p) N_\omega(\boldsymbol{x}, \boldsymbol{z}_p) \Big) + o(\delta^d)$$

for $\boldsymbol{x} \in \partial\Omega$.

Combining (2.9) and Lemma 2.1, the following corollary immediately holds.

Corollary 2.3 *For any* $\boldsymbol{x} \in \partial\Omega$,

$$(-\frac{1}{2}\mathcal{I} + \mathcal{K}_\Omega^\omega)[u - U](\boldsymbol{x}) = -\delta^d \Big(\nabla U(\boldsymbol{z}_a)^T \mathbf{M}(1/\rho, B) \nabla_{\boldsymbol{z}} \Gamma_\omega(\boldsymbol{x} - \boldsymbol{z}_a) + \omega^2 (K^{-1} - 1) |B| U(\boldsymbol{z}_a) \Gamma_\omega(\boldsymbol{x} - \boldsymbol{z}_a) \Big) + o(\delta^d). \tag{2.12}$$

Note that the remainders in expansions (2.9), (2.11), and (2.12) are uniform with respect to $\boldsymbol{x} \in \Omega$ and hold only when the distance between $\boldsymbol{z}_a$ and $\partial\Omega$ is much larger than δ.

2.3 Direct Imaging Algorithms

2.3.1 Direct Imaging at a Fixed Frequency

In this section, we apply the asymptotic formulas (2.9) and (2.11) for the purpose of identifying the location and certain properties of the shape of the acoustic anomalies.

Consider P well-separated anomalies $D_p = \boldsymbol{z}_p + \delta B_p$, $p = 1, \ldots, P$. The volumetric mass density and bulk modulus of D_p are denoted by ρ_p and K_p, respectively. Suppose that all the domains B_p are disks.

MUSIC-Type Algorithm

Let $(\boldsymbol{\theta}_1, \ldots, \boldsymbol{\theta}_n)$ be n unit vectors in $\mathbb{R}^d$. For $\boldsymbol{\theta} \in \{\boldsymbol{\theta}_1, \ldots, \boldsymbol{\theta}_n\}$, we assume that we are in possession of the boundary data u when the domain Ω is illuminated with the plane wave $U(\boldsymbol{x}) = e^{i\omega \boldsymbol{\theta}^T \boldsymbol{x}}$. Therefore, taking the harmonic function $w(\boldsymbol{x}) = e^{-i\omega \boldsymbol{\theta}'^T \boldsymbol{x}}$ for $\boldsymbol{\theta}' \in \{\boldsymbol{\theta}_1, \ldots, \boldsymbol{\theta}_n\}$ and using (2.5) shows that the weighted boundary measurement is approximately equal to

$$I_w[U, \omega] \simeq -\sum_{p=1}^{P} |D_p| \omega^2 \Big(2 \frac{\rho_p^{-1} - 1}{\rho_p^{-1} + 1} \boldsymbol{\theta}^T \boldsymbol{\theta}' + K_p^{-1} - 1 \Big) e^{i\omega (\boldsymbol{\theta} - \boldsymbol{\theta}')^T \boldsymbol{z}_p}.$$

Define the response matrix $\mathbf{A} = (A_{ll'})_{l,l'=1}^n \in \mathbb{C}^{n \times n}$ by

$$A_{ll'} := I_{w_{l'}}[U_l, \omega], \tag{2.13}$$

where $U_l(\boldsymbol{x}) = e^{i\omega \boldsymbol{\theta}_l^T \boldsymbol{x}}$, $w_l(\boldsymbol{x}) = e^{-i\omega \boldsymbol{\theta}_l^T \boldsymbol{x}}$, $l = 1, \ldots, n$. It is approximately given by

$$A_{ll'} \simeq -\sum_{p=1}^{P} |D_p| \omega^2 \Big(2 \frac{\rho_p^{-1} - 1}{\rho_p^{-1} + 1} \boldsymbol{\theta}_l^T \boldsymbol{\theta}_{l'} + K_p^{-1} - 1 \Big) e^{i\omega (\boldsymbol{\theta}_l - \boldsymbol{\theta}_{l'})^T \boldsymbol{z}_p},$$

for $l, l' = 1, \ldots, n$. Introduce the n-dimensional vector fields $\boldsymbol{g}^{(j)}$, defined for $j = 1, \ldots, d+1$, by

$$\boldsymbol{g}^{(j)}(\boldsymbol{x}) = \frac{1}{\sqrt{n}} \big(\boldsymbol{e}_j^T \boldsymbol{\theta}_1 e^{i\omega \boldsymbol{\theta}_1^T \boldsymbol{x}}, \ldots, \boldsymbol{e}_j^T \boldsymbol{\theta}_n e^{i\omega \boldsymbol{\theta}_n^T \boldsymbol{x}} \big)^T, \quad j = 1, \ldots, d, \tag{2.14}$$

and

$$\boldsymbol{g}^{(d+1)}(\boldsymbol{x}) = \frac{1}{\sqrt{n}} \big(e^{i\omega \boldsymbol{\theta}_1^T \boldsymbol{x}}, \ldots, e^{i\omega \boldsymbol{\theta}_n^T \boldsymbol{x}} \big)^T, \tag{2.15}$$

where $(\boldsymbol{e}_1, \ldots, \boldsymbol{e}_d)$ is an orthonormal basis of $\mathbb{R}^d$. Let $\mathbf{P}_{\text{noise}} = \mathbf{I} - \mathbf{P}$, where $\mathbf{P}$ is the orthogonal projection onto the range of $\mathbf{A}$. The MUSIC-type imaging functional is defined by

$$\mathcal{I}_{\mathrm{MU}}(\boldsymbol{z}^S,\omega) := \Big(\sum_{j=1}^{d+1} \|\mathbf{P}_{\mathrm{noise}}\boldsymbol{g}^{(j)}(\boldsymbol{z}^S)\|^2\Big)^{-1/2}. \tag{2.16}$$

This functional has large peaks only at the locations of the anomalies; see, *e.g.*, [1].

Backpropagation-Type Algorithms

Let $(\boldsymbol{\theta}_1,\ldots,\boldsymbol{\theta}_n)$ be n unit vectors in $\mathbb{R}^d$. A backpropagation-type imaging functional at a single frequency ω is given by

$$\mathcal{I}_{\mathrm{BP}}(\boldsymbol{z}^S,\omega) := \frac{1}{n}\sum_{l=1}^{n} e^{-2i\omega\boldsymbol{\theta}_l^T\boldsymbol{z}^S} I_{w_l}[U_l,\omega], \tag{2.17}$$

where $U_l(\boldsymbol{x}) = w_l(\boldsymbol{x}) = e^{i\omega\boldsymbol{\theta}_l^T\boldsymbol{x}}$, $l=1,\ldots,n$. Suppose that $(\boldsymbol{\theta}_1,\ldots,\boldsymbol{\theta}_n)$ are equidistant points on the unit sphere S^{d-1}. For sufficiently large n, we have

$$\frac{1}{n}\sum_{l=1}^{n} e^{i\omega\boldsymbol{\theta}_l^T\boldsymbol{x}} \simeq 4(\frac{\pi}{\omega})^{d-2}\,\mathrm{Im}\big\{\Gamma_\omega(\boldsymbol{x})\big\} = \begin{cases} \mathrm{sinc}(\omega|\boldsymbol{x}|) & \text{for } d=3,\\ J_0(\omega|\boldsymbol{x}|) & \text{for } d=2, \end{cases} \tag{2.18}$$

where $\mathrm{sinc}(s) = \sin(s)/s$ is the sinc function and J_0 is the Bessel function of the first kind and of order zero.

Therefore, it follows that

$$\mathcal{I}_{\mathrm{BP}}(\boldsymbol{z}^S,\omega) \simeq \sum_{p=1}^{P} |D_p|\omega^2\Big(2\frac{\rho_p^{-1}-1}{\rho_p^{-1}+1} - (K_p^{-1}-1)\Big) \times \begin{cases} \mathrm{sinc}(2\omega|\boldsymbol{z}^S-\boldsymbol{z}_p|) & \text{for } d=3,\\ J_0(2\omega|\boldsymbol{z}^S-\boldsymbol{z}_p|) & \text{for } d=2. \end{cases}$$

These formulae show that the resolution of the imaging functional is the standard diffraction limit. It is of the order of half the wavelength $\lambda = 2\pi/\omega$. Note that the above backpropagation-type algorithm is a simplified version of the algorithm studied in [4,5]. In fact, instead of using only the diagonal terms of the response matrix $\mathbf{A}$, defined by (2.13), we can use the whole matrix to define the Kirchhoff migration functional:

$$\mathcal{I}_{\mathrm{KM}}(\boldsymbol{z}^S,\omega) = \sum_{j=1}^{d+1} \overline{\boldsymbol{g}^{(j)}(\boldsymbol{z}^S)}^T \mathbf{A}\boldsymbol{g}^{(j)}(\boldsymbol{z}^S), \tag{2.19}$$

where $\boldsymbol{g}^{(j)}$ are defined by (2.14) and (2.15).

Suppose for simplicity that $P=1$ and $\rho=1$. In this case the response matrix is

$$\mathbf{A} = -n|D|\omega^2(K^{-1}-1)\boldsymbol{g}^{(d+1)}(\boldsymbol{z}_a)\overline{\boldsymbol{g}^{(d+1)}(\boldsymbol{z}_a)}^T$$

and we can prove that $\mathcal{I}_{\mathrm{MU}}$ is a nonlinear pointwise function of $\mathcal{I}_{\mathrm{KM}}$ [4]. In fact, we have

$$\mathcal{I}_{\mathrm{KM}}(\boldsymbol{z}^S,\omega) = -n|D|\omega^2(K^{-1}-1)\Big(1-\mathcal{I}_{\mathrm{MU}}^{-2}(\boldsymbol{z}^S,\omega)\Big).$$

It is worth pointing out that this transformation does not improve neither the stability nor the resolution.

Moreover, in the presence of additive measurement noise, the response matrix can be written as

$$\mathbf{A} = -n|D|\omega^2(K^{-1}-1)\boldsymbol{g}^{(d+1)}(\boldsymbol{z}_a)\overline{\boldsymbol{g}^{(d+1)}(\boldsymbol{z}_a)}^T + \sigma\omega\mathbf{W},$$

where $\mathbf{W}$ is a complex symmetric Gaussian matrix with mean zero and variance 1. According to [4], the Signal-to-Noise Ratio (SNR) of the imaging functional $\mathcal{I}_{\mathrm{KM}}$, defined by

$$\mathrm{SNR}(\mathcal{I}_{\mathrm{KM}}) = \frac{\mathbb{E}[\mathcal{I}_{\mathrm{KM}}(\boldsymbol{z}_a,\omega)]}{\mathrm{Var}(\mathcal{I}_{\mathrm{KM}}(\boldsymbol{z}_a,\omega))^{1/2}},$$

is then equal to

$$\mathrm{SNR}(\mathcal{I}_{\mathrm{KM}}) = \frac{n\omega|D|\,|K^{-1}-1|}{\sigma}. \tag{2.20}$$

For the MUSIC algorithm, the peak of $\mathcal{I}_{\mathrm{MU}}$ is affected by measurement noise. We have [16]

$$\mathcal{I}_{\mathrm{MU}}(\boldsymbol{z}_a,\omega) = \begin{cases} \frac{n|D|\omega|K^{-1}-1|}{\sigma} & \text{if } n|D|\omega|K^{-1}-1| \gg \sigma, \\ 1 \quad \text{if } n|D|\omega|K^{-1}-1| \ll \sigma. \end{cases}$$

Suppose now that the medium is randomly heterogeneous around a constant background. Let K be the bulk modulus of the anomaly D. The index of refraction is of the form $1+(K^{-1}-1)\mathbf{1}_D(\boldsymbol{x})+\mu(\boldsymbol{x})$, where 1 stands for the constant background, $(K^{-1}-1)\mathbf{1}_D(\boldsymbol{x})$ stands for the localized perturbation of the index of refraction due to the anomaly, and $\mu(\boldsymbol{x})$ stands for the fluctuations of the index of refraction due to clutter (*i.e.*, medium noise). We assume that μ is a random process with Gaussian statistics and mean zero, and that it is compactly supported within Ω.

If the random process μ has a small amplitude, then the background solution U, *i.e.*, the field that would be observed without the anomaly, can be approximated by

$$U(\boldsymbol{x}) \simeq U^{(0)}(\boldsymbol{x}) - \omega^2\int_\Omega N_\omega^{(0)}(\boldsymbol{x},\boldsymbol{y})\mu(\boldsymbol{y})U^{(0)}(\boldsymbol{y})\,d\boldsymbol{y},$$

where $U^{(0)}$ and $N_\omega^{(0)}$ are respectively the background solution and the Neumann function in the constant background case. On the other hand, in the

weak fluctuation regime, the phase mismatch between $N_\omega(\boldsymbol{x}, \boldsymbol{z}_a)$, the Neumann function in the random background, and $N_\omega^{(0)}(\boldsymbol{x}, \boldsymbol{z}^S)$ when $\boldsymbol{z}^S$ is close to $\boldsymbol{z}_a$ comes from the random fluctuations of the travel time between $\boldsymbol{x}$ and $\boldsymbol{z}_a$ which is approximately equal to the integral of $\mu/2$ along the ray from $\boldsymbol{x}$ to $\boldsymbol{z}_a$:

$$N_\omega(\boldsymbol{x}, \boldsymbol{z}_a) \simeq N_\omega^{(0)}(\boldsymbol{x}, \boldsymbol{z}_a) e^{i\omega T(\boldsymbol{x})},$$

with

$$T(\boldsymbol{x}) \simeq \frac{|\boldsymbol{x} - \boldsymbol{z}_a|}{2} \int_0^1 \mu\Big(\boldsymbol{z}_a + \frac{\boldsymbol{x} - \boldsymbol{z}_a}{|\boldsymbol{x} - \boldsymbol{z}_a|} s\Big)\, ds.$$

Therefore, for any smooth function w satisfying $(\Delta + \omega^2)w = 0$ in Ω, the weighted boundary measurements $I_w[U^{(0)}, \omega]$, defined by (2.10), is approximately given by

$$\begin{aligned} I_w[U^{(0)}, \omega] \simeq & -|D|\omega^2 (K^{-1} - 1) e^{-\frac{\omega^2 \mathrm{Var}(T)}{2}} w(\boldsymbol{z}_a) U^{(0)}(\boldsymbol{z}_a) \\ & -\omega^2 \int_\Omega w(\boldsymbol{y}) U^{(0)}(\boldsymbol{y}) \mu(\boldsymbol{y})\, d\boldsymbol{y}, \end{aligned} \tag{2.21}$$

provided that the correlation radius of the random process μ is small [3]. Expansion (2.21) shows that the medium noise reduces the height of the main peak of $\mathcal{I}_{\mathrm{KM}}$ by the damping factor $e^{-\omega^2 \mathrm{Var}(T)/2}$ and on the other hand it induces random fluctuations of the associated image in the form of a speckle field.

Topological Derivative Based Imaging Functional

The topological derivative based imaging functional was introduced in [3].

Let $D' = \boldsymbol{z}^S + \delta' B'$, $K' > 1$, $\rho' > 1$, B' be chosen a priori, and let δ' be small. If $K < 1$ and $\rho < 1$, then we choose $K' < 1$ and $\rho' < 1$.

Let w be the solution of the Helmholtz equation

$$\begin{cases} \Delta w + \omega^2 w = 0 \quad \text{in } \Omega, \\ \dfrac{\partial w}{\partial \nu} = (-\dfrac{1}{2}\mathcal{I} + (\mathcal{K}_\Omega^{-\omega})^*)\overline{(-\dfrac{1}{2}\mathcal{I} + \mathcal{K}_\Omega^{\omega})[U - u_{\mathrm{meas}}]} \quad \text{on } \partial\Omega, \end{cases} \tag{2.22}$$

where u_{meas} is the boundary pressure in the presence of the acoustic anomaly. The function w is obtained by backpropagating the Neumann data

$$(-\frac{1}{2}\mathcal{I} + (\mathcal{K}_\Omega^{\omega})^*)(-\frac{1}{2}\mathcal{I} + \mathcal{K}_\Omega^{\omega})[U - u_{\mathrm{meas}}]$$

inside the background medium (without any anomaly). Note that $\overline{(\mathcal{K}_\Omega^{\omega})^*} = (\mathcal{K}_\Omega^{-\omega})^*$.

The function w can be used to image the anomaly. It corresponds to backpropagating the discrepancy between the measured and the background solutions. However, we introduce here a functional that exploits better the coherence between the phases of the background and perturbed fields at the location of the anomaly. This functional turns out to be exactly the topological derivative imaging functional introduced [3].

For a single measurement, we set

$$\mathcal{I}_{\mathrm{TD}}[U](\boldsymbol{z}^S) = \mathrm{Re}\Big\{ \nabla U(\boldsymbol{z}^S)^T \mathbf{M}(1/\rho', B') \nabla w(\boldsymbol{z}^S) + \omega^2 (K'^{-1} - 1)|B'| U(\boldsymbol{z}^S) w(\boldsymbol{z}^S) \Big\}. \tag{2.23}$$

The functional $\mathcal{I}_{\mathrm{TD}}[U](\boldsymbol{z}^S)$ gives, at every search point $\boldsymbol{z}^S \in \Omega$, the sensitivity of the misfit function

$$\mathcal{E}[U](\boldsymbol{z}^S) := \frac{1}{2} \int_{\partial\Omega} \left| (-\frac{1}{2}\mathcal{I} + \mathcal{K}_\Omega^\omega)[u_{\boldsymbol{z}^S} - u_{\mathrm{meas}}](\boldsymbol{x}) \right|^2 d\sigma(\boldsymbol{x}),$$

where $u_{\boldsymbol{z}^S}$ is the solution of (2.1) with the anomaly $D' = \boldsymbol{z}^S + \delta' B'$. The location of the maximum of $\boldsymbol{z}^S \mapsto \mathcal{I}_{\mathrm{TD}}[U](\boldsymbol{z}^S)$ corresponds to the point at which the insertion of an anomaly centered at that point maximally decreases the misfit function. Using Corollary 2.3, we can show that the functional $\mathcal{I}_{\mathrm{TD}}$ attains its maximum at $\boldsymbol{z}^S = \boldsymbol{z}_a$; see [3]. It is also shown in [3] that the postprocessing of the data set by applying the integral operator $(-\frac{1}{2}\mathcal{I} + \mathcal{K}_\Omega^\omega)$ is essential in order to obtain an efficient topological based imaging functional, both in terms of resolution and stability. By postprocessing the data, we ensure that the topological based imaging functional attains its maximum at the true location of the anomaly.

For multiple measurements, $U_l, l = 1, \ldots, n$, the topological derivative based imaging functional is simply given by

$$\mathcal{I}_{\mathrm{TD}}(\boldsymbol{z}^S, \omega) := \frac{1}{n} \sum_{l=1}^{n} \mathcal{I}_{\mathrm{TD}}[U_l](\boldsymbol{z}^S). \tag{2.24}$$

Let, for simplicity, $(\boldsymbol{\theta}_1, \ldots, \boldsymbol{\theta}_n)$ be n uniformly distributed directions over the unit sphere and consider U_l to be the plane wave

$$U_l(\boldsymbol{x}) = e^{i\omega \boldsymbol{\theta}_l^T \boldsymbol{x}}, \quad \boldsymbol{x} \in \Omega, \quad l = 1, \ldots, n. \tag{2.25}$$

Let

$$r_\omega(\boldsymbol{z}^S, \boldsymbol{z}) := \int_{\partial\Omega} \Gamma_\omega(\boldsymbol{x} - \boldsymbol{z}^S) \overline{\Gamma_\omega}(\boldsymbol{x} - \boldsymbol{z})\, d\sigma(\boldsymbol{x}), \tag{2.26}$$

$$\mathbf{R}_\omega(\boldsymbol{z}^S, \boldsymbol{z}) := \int_{\partial\Omega} \nabla_{\boldsymbol{z}} \Gamma_\omega(\boldsymbol{x} - \boldsymbol{z}^S) \nabla_{\boldsymbol{z}} \overline{\Gamma_\omega}(\boldsymbol{x} - \boldsymbol{z})^T\, d\sigma(\boldsymbol{x}). \tag{2.27}$$

Note that $\mathbf{R}_\omega(\boldsymbol{z}^S, \boldsymbol{z})$ is a $d \times d$ matrix. When $\rho = 1$, we have

$$\mathcal{I}_{\mathrm{TD}}[U](\boldsymbol{z}^S) \simeq \delta^d \omega^4 (K'^{-1} - 1)(K^{-1} - 1)|B'| \mathrm{Re}\Big\{ U(\boldsymbol{z}^S) r_\omega(\boldsymbol{z}^S, \boldsymbol{z}_a) \overline{U}(\boldsymbol{z}_a) \Big\}, \tag{2.28}$$

where r_ω is given by (2.26). Therefore, by computing the topological derivatives for the n plane waves (n sufficiently large), it follows from (2.18) together with

$$\int_{\partial\Omega} \overline{\Gamma_\omega}(\boldsymbol{x} - \boldsymbol{z}) \Gamma_\omega(\boldsymbol{x} - \boldsymbol{z}^S)\, d\sigma(\boldsymbol{x}) \sim \frac{1}{\omega} \mathrm{Im}\big\{ \Gamma_\omega(\boldsymbol{z}^S - \boldsymbol{z}) \big\}, \qquad d = 2, 3, \tag{2.29}$$

where $A \sim B$ means $A \simeq CB$ for some constant C independent of ω, that

$$\frac{1}{n} \sum_{l=1}^{n} \mathcal{I}_{\mathrm{TD}}[U_l](\boldsymbol{z}^S) \sim \omega^{5-d} (\mathrm{Im}\big\{ \Gamma_\omega(\boldsymbol{z}^S - \boldsymbol{z}_a) \big\})^2.$$

Similarly, when $K = 1$, by computing the topological derivatives for the n plane waves, $U_l, l = 1, \ldots, n$, given by (2.25), we obtain

$$\begin{aligned} &\frac{1}{n} \sum_{l=1}^{n} \mathcal{I}_{\mathrm{TD}}[U_l](\boldsymbol{z}^S) \\ &\quad \simeq \delta^d \omega^2 \frac{1}{n} \sum_{l=1}^{n} \mathrm{Re}\big\{ e^{i\omega \boldsymbol{\theta}_l^T (\boldsymbol{z}^S - \boldsymbol{z}_a)} \big[\boldsymbol{\theta}_l^T \mathbf{M}(1/\rho', B') \mathbf{R}_\omega(\boldsymbol{z}^S, \boldsymbol{z}_a) \mathbf{M}(1/\rho, B)^T \boldsymbol{\theta}_l \big] \big\}. \end{aligned}$$

Using $\rho' = 0$ and B' the unit disk, the polarization tensor $\mathbf{M}(1/\rho', B') = C_d \mathbf{I}$, where C_d is a constant, is proportional to the identity [8]. If, additionally, we assume that $\mathbf{M}(1/\rho, B)$ is approximately proportional to the identity, which occurs in particular when B is a disk or a ball, then by using

$$\begin{aligned} &\int_{\partial\Omega} \nabla_{\boldsymbol{z}} \Gamma_\omega(\boldsymbol{x} - \boldsymbol{z}^S) \nabla_{\boldsymbol{z}} \overline{\Gamma_\omega}(\boldsymbol{x} - \boldsymbol{z})^T\, d\sigma(\boldsymbol{x}) \\ &\qquad \sim \omega\, \mathrm{Im}\big\{ \Gamma_\omega(\boldsymbol{z}^S - \boldsymbol{z}) \big\} \left(\frac{\boldsymbol{z} - \boldsymbol{z}^S}{|\boldsymbol{z} - \boldsymbol{z}^S|} \right) \left(\frac{\boldsymbol{z} - \boldsymbol{z}^S}{|\boldsymbol{z} - \boldsymbol{z}^S|} \right)^T, \end{aligned} \tag{2.30}$$

we arrive at

$$\frac{1}{n} \sum_{l=1}^{n} \mathcal{I}_{\mathrm{TD}}[U_l](\boldsymbol{z}^S) \sim \omega^{5-d} (\mathrm{Im}\big\{ \Gamma_\omega(\boldsymbol{z}^S - \boldsymbol{z}_a) \big\})^2. \tag{2.31}$$

Therefore, $\mathcal{I}_{\mathrm{TD}}$ attains its maximum at $\boldsymbol{z}_a$. Moreover, the resolution for the location estimation is given by the diffraction limit. We refer the reader to [3] for a detailed stability analysis of $\mathcal{I}_{\mathrm{TD}}$ with respect to both medium and measurement noises as well as its resolution. In the case of measurement noise, the SNR of $\mathcal{I}_{\mathrm{TD}}$,

$$\mathrm{SNR}(\mathcal{I}_{\mathrm{TD}}) = \frac{\mathbb{E}[\mathcal{I}_{\mathrm{TD}}(\boldsymbol{z}_a,\omega)]}{\mathrm{Var}(\mathcal{I}_{\mathrm{TD}}(\boldsymbol{z}_a,\omega))^{1/2}},$$

is equal to

$$\mathrm{SNR}(\mathcal{I}_{\mathrm{TD}}) = \frac{\sqrt{2}\pi^{1-d/2}\omega^{(d+1)/2}|U(\boldsymbol{z}_a)|(K^{-1}-1)|D|}{\sigma},$$

where σ^2 is the noise variance.

In the case of medium noise, let us introduce the kernel

$$Q(\boldsymbol{z}^S,\boldsymbol{z}_a) := \mathrm{Re}\Big\{U^{(0)}(\boldsymbol{z}^S)\overline{U^{(0)}(\boldsymbol{z}_a)}\int_{\partial\Omega}\Gamma_\omega(\boldsymbol{x}-\boldsymbol{z}^S)\overline{\Gamma_\omega(\boldsymbol{x}-\boldsymbol{z}_a)}\,d\sigma(\boldsymbol{x})\Big\}.$$

We can express the topological derivative imaging functional as follows [3]:

$$\begin{aligned}\mathcal{I}_{\mathrm{TD}}[U^{(0)}](\boldsymbol{z}^S) \simeq{}& \omega^4({K'}^{-1}-1)|B'|\int_\Omega \mu(\boldsymbol{y})Q(\boldsymbol{z}^S,\boldsymbol{y})\,d\boldsymbol{y}\\ &+\omega^4({K'}^{-1}-1)(K^{-1}-1)|B'||D|Q(\boldsymbol{z}^S,\boldsymbol{z}_a)e^{-\frac{\omega^2\mathrm{Var}(T)}{2}},\end{aligned} \tag{2.32}$$

provided, once again, that the correlation radius of the random process μ is small. Consequently, the topological derivative has the form of a peak centered at the location $\boldsymbol{z}_a$ of the anomaly (second term of the right-hand side of (2.32)) buried in a zero-mean Gaussian field or speckle pattern (first term of the right-hand side of (2.32)) that we can characterize statistically.

2.3.2 Direct Imaging at Multiple Frequencies

Let $(\boldsymbol{\theta}_1,\ldots,\boldsymbol{\theta}_n)$ be n uniformly distributed directions over the unit sphere. We consider plane wave illuminations at multiple frequencies, $(\omega_k)_{k=1,\ldots,m}$, instead of a fixed frequency:

$$U_{lk}(\boldsymbol{x}) := U(\boldsymbol{x},\boldsymbol{\theta}_l,\omega_k) = e^{i\omega_k\boldsymbol{\theta}_l^T\boldsymbol{x}},$$

and record the acoustic perturbations due to the anomaly. In this case, we can construct the topological derivative imaging functional by summing over frequencies

$$\mathcal{I}_{\mathrm{TDF}}(\boldsymbol{z}^S) := \frac{1}{m}\sum_{k=1}^{m}\mathcal{I}_{\mathrm{TD}}(\boldsymbol{z}^S,\omega_k). \tag{2.33}$$

Suppose for simplicity that $\rho = 1$. Then, (2.28) and (2.29) yield

$$\mathcal{I}_{\mathrm{TDF}}(\boldsymbol{z}^S) \sim \int_\omega \omega^{5-d}\Big(\mathrm{Im}\big\{\Gamma_\omega(\boldsymbol{z}^S-\boldsymbol{z}_a)\big\}\Big)^2 d\omega, \quad d=2,3,$$

and hence, $\mathcal{I}_{\mathrm{TDF}}(\boldsymbol{z}^S)$ has a large peak only at $\boldsymbol{z}_a$. In the general case, we can use (2.30) to state the same behavior at $\boldsymbol{z}_a$.

An alternative imaging functional when searching for an anomaly using multiple frequencies is the reverse time migration imaging functional [11]:

$$\mathcal{I}_{\mathrm{RMF}}(\boldsymbol{z}^S) := \frac{1}{nm}\sum_{l=1}^{n}\sum_{k=1}^{m}\overline{U}(\boldsymbol{z}^S,\boldsymbol{\theta}_l,\omega_k) \times \int_{\partial\Omega}(-\frac{\mathcal{I}}{2}+\mathcal{K}_\Omega^{\omega_k})(u-U)(\boldsymbol{x},\boldsymbol{\theta}_l,\omega_k)\overline{\Gamma_{\omega_k}}(\boldsymbol{x},\boldsymbol{z}^S)\,d\sigma(\boldsymbol{x}). \tag{2.34}$$

In fact, when for instance $\rho = 1$,

$$\mathcal{I}_{\mathrm{RMF}}(\boldsymbol{z}^S) \sim \frac{1}{nm}\sum_{l=1}^{m}\sum_{k=1}^{m}\omega_k^3 U(\boldsymbol{z}_a,\boldsymbol{\theta}_l,\omega_k)\overline{U}(\boldsymbol{z}^S,\boldsymbol{\theta}_l,\omega_k)\mathrm{Im}\{\Gamma_{\omega_k}(\boldsymbol{z}^S-\boldsymbol{z}_a)\},$$

and therefore, it is approximately proportional to

$$\int_{\mathcal{S}^{d-1}}\int_\omega \omega^3 e^{i\omega\boldsymbol{\theta}^T(\boldsymbol{z}^S-\boldsymbol{z}_a)}\mathrm{Im}\{\Gamma_\omega(\boldsymbol{z}^S-\boldsymbol{z}_a)\}d\omega d\sigma(\boldsymbol{\theta}) \sim \int_\omega \omega^{5-d}\Big(\mathrm{Im}\{\Gamma_\omega(\boldsymbol{z}^S-\boldsymbol{z}_a)\}\Big)^2 d\omega,$$

where $\mathcal{S}^{d-1}$ is the unit sphere and $d = 2, 3$. Hence,

$$\mathcal{I}_{\mathrm{RMF}}(\boldsymbol{z}^S) \sim \mathcal{I}_{\mathrm{TDF}}(\boldsymbol{z}^S).$$

Finally, it is also possible to use a backpropagation imaging functional:

$$\mathcal{I}_{\mathrm{BPF}}(\boldsymbol{z}^S) := \frac{1}{m}\sum_{k=1}^{m}\mathcal{I}_{\mathrm{BP}}(\boldsymbol{z}^S,\omega),$$

or a Kirchhoff imaging functional:

$$\mathcal{I}_{\mathrm{KMF}}(\boldsymbol{z}^S) := \frac{1}{m}\sum_{k=1}^{m}\mathcal{I}_{\mathrm{KM}}(\boldsymbol{z}^S,\omega).$$

We contrast this with the matched field imaging functional:

$$\mathcal{I}_{\mathrm{MF}}(\boldsymbol{z}^S) := \frac{1}{m}\sum_{k=1}^{m}|\mathcal{I}_{\mathrm{KM}}(\boldsymbol{z}^S,\omega)|^2,$$

in which the phase coherence between the different frequency-dependent acoustic perturbations is not exploited. This makes sense when the different frequency-dependent perturbations are incoherent.

If the measurement noises $\nu_{\mathrm{noise}}(\boldsymbol{x},\omega_k), k = 1,\ldots,m$, are independent and identically distributed, the multiple frequencies enhance the detection performance via a higher "effective" SNR.

If some correlation between frequency-dependent perturbations exist, for example because of a medium noise, then summing over frequencies an imaging functional is not appropriate. A single-frequency imaging functional at the frequency which maximizes the SNR may give a better reconstruction.

In the presence of a medium noise, a CINT procedure may be appropriate. Following [13,14] a CINT-like algorithm is given by

$$\begin{aligned}\mathcal{I}_{\mathrm{CINT}}(\boldsymbol{z}^S) = \int_{\mathcal{S}^{d-1}}\int_{\omega_1}\int_{\omega_2}\int_{\partial\Omega}\int_{\partial\Omega} & e^{-\frac{|\omega_1-\omega_2|^2}{2\Omega_D^2}} e^{-\frac{|\boldsymbol{x}_1-\boldsymbol{x}_2|^2}{2X_D^2}} \\ & \times (-\frac{\mathcal{I}}{2}+\mathcal{K}_\Omega^{\omega_1})(u-U)(\boldsymbol{x}_1,\boldsymbol{\theta},\omega_1)\overline{\Gamma_{\omega_1}}(\boldsymbol{x}_1,\boldsymbol{z}^S)\overline{U}(\boldsymbol{z}^S,\boldsymbol{\theta},\omega_1) \\ & \times \overline{(-\frac{\mathcal{I}}{2}+\mathcal{K}_\Omega^{\omega_2})(u-U)}(\boldsymbol{x}_2,\boldsymbol{\theta},\omega_2)\Gamma_{\omega_2}(\boldsymbol{x}_2,\boldsymbol{z}^S) \\ & \times U(\boldsymbol{z}^S,\boldsymbol{\theta},\omega_2)d\sigma(\boldsymbol{x})d\omega_1 d\omega_2 d\sigma(\boldsymbol{\theta}), \end{aligned} \tag{2.35}$$

where X_D and Ω_D are two cut-off parameters.

The purpose of the CINT-like imaging functional $\mathcal{I}_{\mathrm{CINT}}$ is to keep in (2.35) the pairs $(\boldsymbol{x}_1,\omega_1)$ and $(\boldsymbol{x}_2,\omega_2)$ for which the postprocessed data $(-\frac{1}{2}\mathcal{I}+\mathcal{K}_\Omega^{\omega_1})[u-U](\boldsymbol{x}_1,\omega_1)$ and $(-\frac{1}{2}\mathcal{I}+\mathcal{K}_\Omega^{\omega_2})[u-U](\boldsymbol{x}_1,\omega_1)$ are coherent, and to remove the pairs that do not bring information.

Depending on the parameters X_D, Ω_D, we get different trade-offs between resolution and stability. When X_D and Ω_D become small, $\mathcal{I}_{\mathrm{CINT}}$ presents better stability properties at the expense of a loss of resolution. In the limit $X_D \to \infty$, $\Omega_D \to \infty$, we get the square of the topological derivative functional $\mathcal{I}_{\mathrm{TDF}}$. A precise stability and resolution analysis for $\mathcal{I}_{\mathrm{CINT}}$ can be derived by exactly the same arguments as those in [2].

2.4 Numerical Illustrations

In this section we present results of numerical experiments to illustrate the performance of the imaging functionals introduced in the previous section.

We consider the two-dimensional case ($d = 2$). The domain Ω is the unit disk. We simulate the measurements using a finite-element method to solve the Helmholtz equation. We use a piecewise linear representation of the solution u and piecewise constant representations of the parameter distributions $\mathbf{1}_{\Omega\setminus\overline{D}}(\boldsymbol{x})+\rho^{-1}\mathbf{1}_D(\boldsymbol{x})$ and $\mathbf{1}_{\Omega\setminus\overline{D}}(\boldsymbol{x})+K^{-1}\mathbf{1}_D(\boldsymbol{x})$. We consider a small anomaly $D = \boldsymbol{z}_a + \delta B$ with $\boldsymbol{z}_a = (-0.3, 0.5)$, $\delta = 0.05$, and B being the unit disk.

2.4.1 Measurements at a Fixed Frequency

We fix the working frequency ω to be equal to 6, which corresponds to a wavelength $\lambda \simeq 1$. We assume that the measurements correspond to the plane wave illuminations, $U_l(\boldsymbol{x}) = e^{i\omega\boldsymbol{\theta}_l^T\boldsymbol{x}}$, at the equi-distributed directions $\boldsymbol{\theta}_l$, for $l = 1,\ldots,n = 50$.

Bulk Modulus Contrast Only

Here, the parameters of the anomaly are $\rho = 1$ and $K = 1/2$.

Resolution in the Absence of Noise

Within the above setting, we first present results of the described algorithms in the absence of noise. In Fig. 2.1, plots of $\mathcal{I}_{\mathrm{TD}}(\boldsymbol{z}^S, \omega)$, defined by (2.24), with $n = 50$ and $n = 2$ illustrate the efficiency of the proposed topological derivative based imaging procedure. The imaging functional $\mathcal{I}_{\mathrm{TD}}(\boldsymbol{z}^S, \omega)$ reaches its maximum at the location $\boldsymbol{z}_a$ of the anomaly and behaves, accordingly to (2.30), like $J_0(\omega|\boldsymbol{z}^S - \boldsymbol{z}_a|)^2$ if the number n of incident waves is large while for small n, it behaves, as expected, like $J_0(\omega|\boldsymbol{z}^S - \boldsymbol{z}_a|)$.

In Fig. 2.2, we present two MUSIC-type reconstructions. Given the structure of the response matrix $\mathbf{A}$ with $\rho = 1$ (contrast only on the K distribution), it is known that its SVD yields only one significant singular value. See, *e.g.*, [1,6]. Thus, the illumination vectors $\boldsymbol{g}^{(1)}$ and $\boldsymbol{g}^{(2)}$ (see (2.14)) do not belong to the signal subspace of $\mathbf{A}$. Using these vectors in the projection step generates a blurred MUSIC image (figure on the left). To get a sharp peak, we should project only the illumination vector $\boldsymbol{g}^{(3)}$ (figure on the right), which assumes a priori knowledge of the physical nature of the contrast.

As shown in Fig. 2.3, the backpropagation image of the anomaly has the expected behavior of the Bessel function and reaches its maximum at the location of the anomaly.

Stability with Respect to Measurement and Medium Noises

We now consider imaging at a fixed frequency from noisy data. We first add electronic (measurement) noise ν_{noise} to the previous measurements $u_{i,\mathrm{meas}}$, $i = 1, \ldots, n$. Here, ν_{noise} is a white Gaussian noise with standard

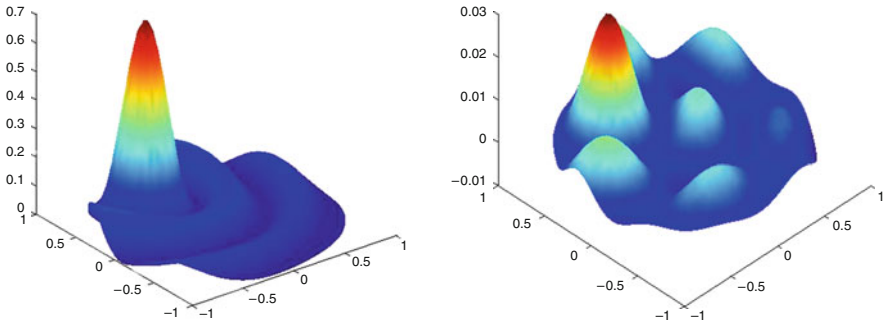

Fig. 2.1. Plots of $\mathcal{I}_{\mathrm{TD}}(\boldsymbol{z}^S, \omega)$ defined by (2.24) with $n = 50$ (*left*) and $n = 2$ (*right*)

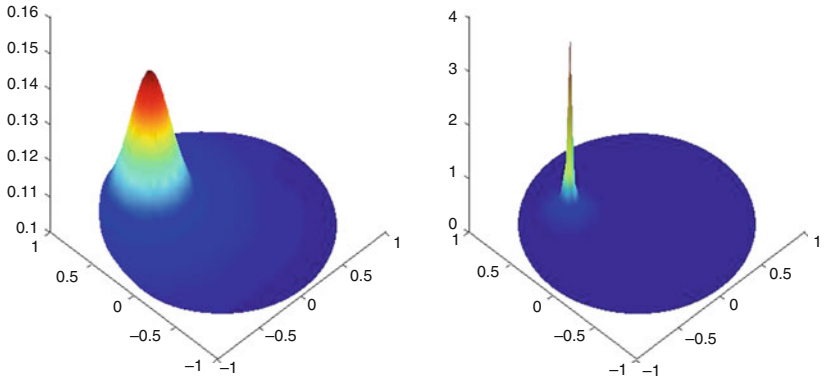

Fig. 2.2. *Left*: MUSIC image using the projection of $\boldsymbol{g}^{(1)}, \boldsymbol{g}^{(2)}$, and $\boldsymbol{g}^{(3)}$ on the signal subspace of $\mathbf{A}$. *Right*: MUSIC image using the projection of $\boldsymbol{g}^{(3)}$ on the signal subspace of $\mathbf{A}$

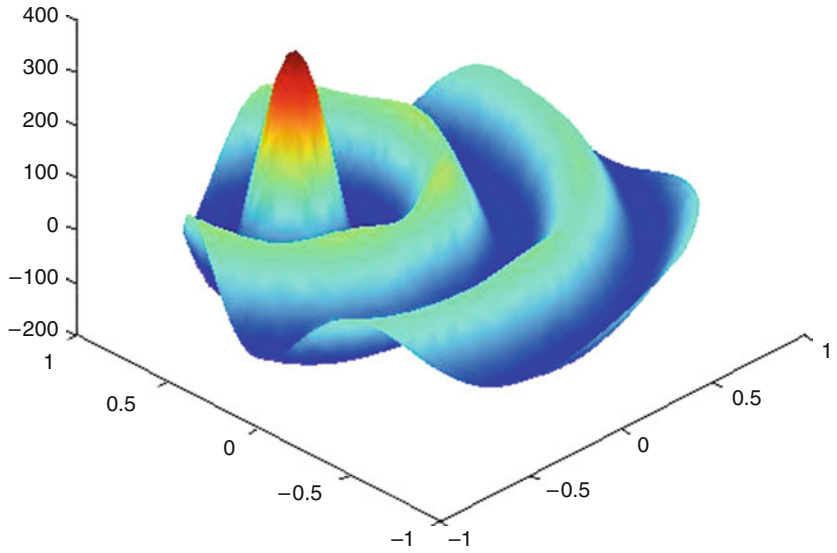

Fig. 2.3. Plot of $\mathcal{I}_{\mathrm{BP}}(\boldsymbol{z}^S, \omega)$ defined by (2.17) with $n = 50$

deviation $\sigma\%$ of the L^2 norm of u_{meas} and σ ranges from 0 to 30. We compute $N_r = 250$ realizations of such noise and apply different imaging algorithms. Figure 2.4 presents the results of computational experiments. It clearly shows that the topological derivative based functional performs as good as Kirchhoff migration and much better than MUSIC and backpropagation, specially at high levels of electronic noise.

We now suppose that the medium bulk modulus is randomly heterogeneous around a constant background: $K^{-1}(\boldsymbol{x}) = 1 + (K^{-1} - 1)\mathbf{1}_D(\boldsymbol{x}) + \mu(\boldsymbol{x})$.

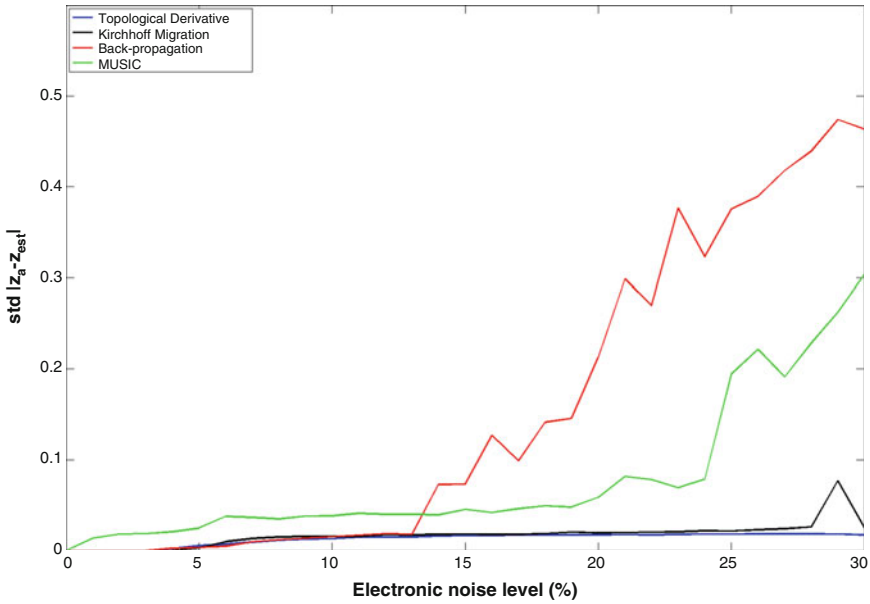

Fig. 2.4. Standard deviations of localization error with respect to electronic noise level for $\mathcal{I}_{\text{MU}}, \mathcal{I}_{\text{BP}}, \mathcal{I}_{\text{KM}}$, and $\mathcal{I}_{\text{TD}}$ with $n = 50$

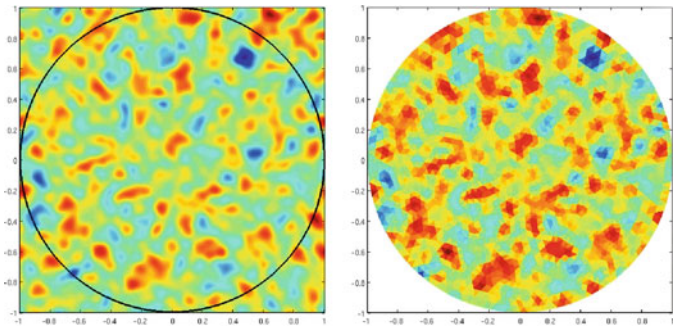

Fig. 2.5. Realization of a medium noise

To simulate μ, we first generate on a grid a white Gaussian noise. Then we filter the Gaussian noise in the Fourier domain by applying a low-pass wavenumber filter. The parameters of the filter are linked to the correlation length l_μ of μ [17]. Figure 2.5 shows a typical realization of a medium noise and its projection on the finite-element mesh.

Comparisons between the standard deviations of the localization error with respect to clutter noise for the discussed imaging algorithms are given in Fig. 2.6. Again, the topological derivative based imaging functional is the most robust functional.

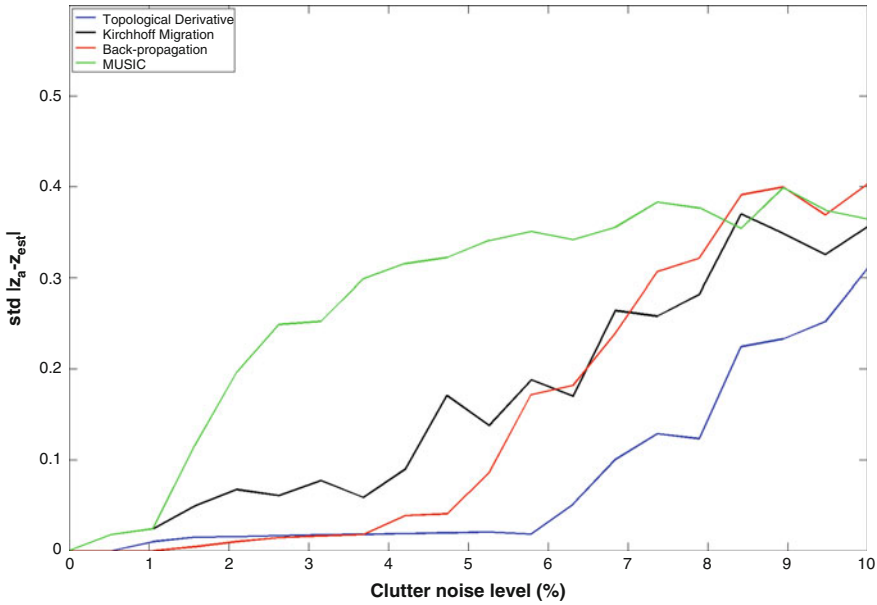

Fig. 2.6. Standard deviations of localization error with respect to clutter noise for $\mathcal{I}_{\mathrm{MU}}, \mathcal{I}_{\mathrm{BP}}, \mathcal{I}_{\mathrm{KM}}$, and $\mathcal{I}_{\mathrm{TD}}$ with $n = 50$

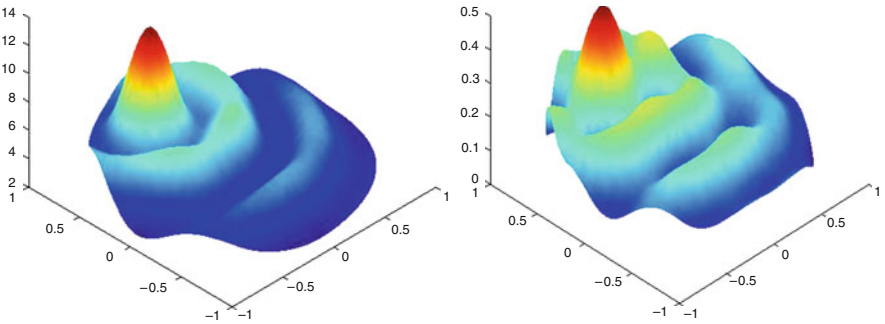

Fig. 2.7. Plots of $\mathcal{I}_{\mathrm{TD}}(\boldsymbol{z}^S, \omega)$ with (*left*) $n = 50$ and (*right*) $n = 2$

Density Contrast Only

Here, the parameters of the anomaly are $\rho = 1/2$ and $K = 1$.

Resolution in the Absence of Noise

As shown in Fig. 2.7, the topological derivative based imaging functional $\mathcal{I}_{\mathrm{TD}}(\boldsymbol{z}^S, \omega)$ reaches its maximum at the location of the anomaly.

Figure 2.8 shows MUSIC images. As expected from the structure of the response matrix with $K = 1$ (ρ contrast only), its SVD yields two significant singular values [1, 6, 15]. Thus, the illumination vector $\boldsymbol{g}^{(3)}$ does not belong to the signal subspace of the response matrix $\mathbf{A}$. As before, using this vector in the projection step generates a blurred MUSIC peak (figure on the left). To get a sharp peak, we should only project the illumination vectors $\boldsymbol{g}^{(1)}$ and $\boldsymbol{g}^{(2)}$ (figure on the right).

As shown in Fig. 2.9, the backpropagation image has the expected behavior and reaches its maximum at the location of the anomaly.

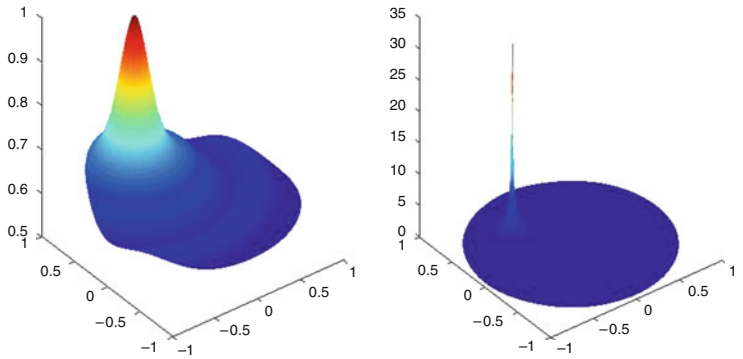

Fig. 2.8. *Left*: MUSIC image using projection of $\boldsymbol{g}^{(1)}, \boldsymbol{g}^{(2)}, \boldsymbol{g}^{(3)}$ on the signal subspace of $\mathbf{A}$. *Right*: image using projection of $\boldsymbol{g}^{(1)}$ and $\boldsymbol{g}^{(2)}$ on the signal subspace of $\mathbf{A}$

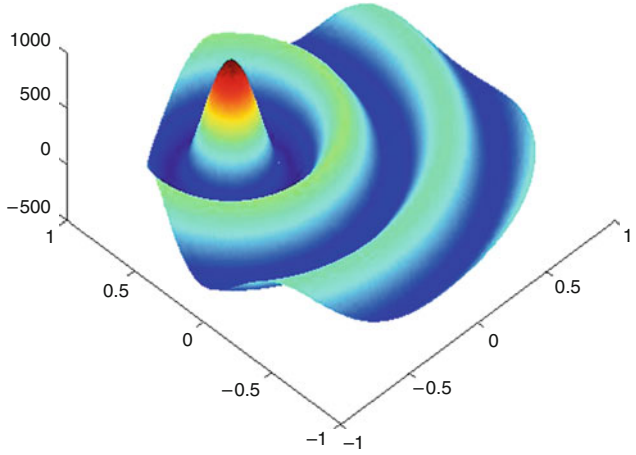

Fig. 2.9. Backpropagation image

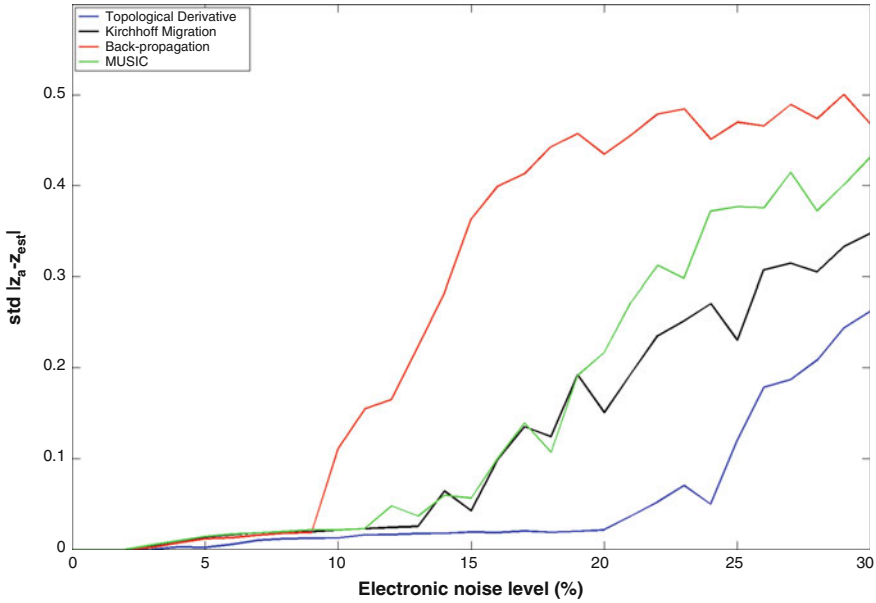

Fig. 2.10. Standard deviations of localization error with respect to electronic noise level for $\mathcal{I}_{\mathrm{MU}}, \mathcal{I}_{\mathrm{BP}}, \mathcal{I}_{\mathrm{KM}}$, and $\mathcal{I}_{\mathrm{TD}}$ with $n = 50$

Stability with Respect to Measurement and Medium Noises

We carry out the same analysis as in the case of only a bulk modulus contrast. Figure 2.10 gives the standard deviation of the localization error as function of the noise level σ for each algorithm.

Again, the topological derivative algorithm seems to be the most robust.

Finally, we suppose that the medium density is randomly heterogeneous around a constant background: $\rho^{-1}(\boldsymbol{x}) = 1 + (\rho^{-1} - 1)\mathbf{1}_D(\boldsymbol{x}) + \mu(\boldsymbol{x})$, with μ a random process of mean zero and tunable standard deviation σ. As before, we compute $N_r = 250$ realizations of such clutter and the corresponding measurements. We then apply the localization algorithms. Stability results are given in Fig. 2.11. They clearly indicate the robustness of the topological derivative based imaging functional.

2.4.2 Measurements at Multiple Frequencies

We illustrate the multifrequency approach with a bulk modulus contrast inclusion. We choose $m = 30$ frequencies between 0 and $\omega_M = 6$ and keep $n = 50$ equidistributed illuminations.

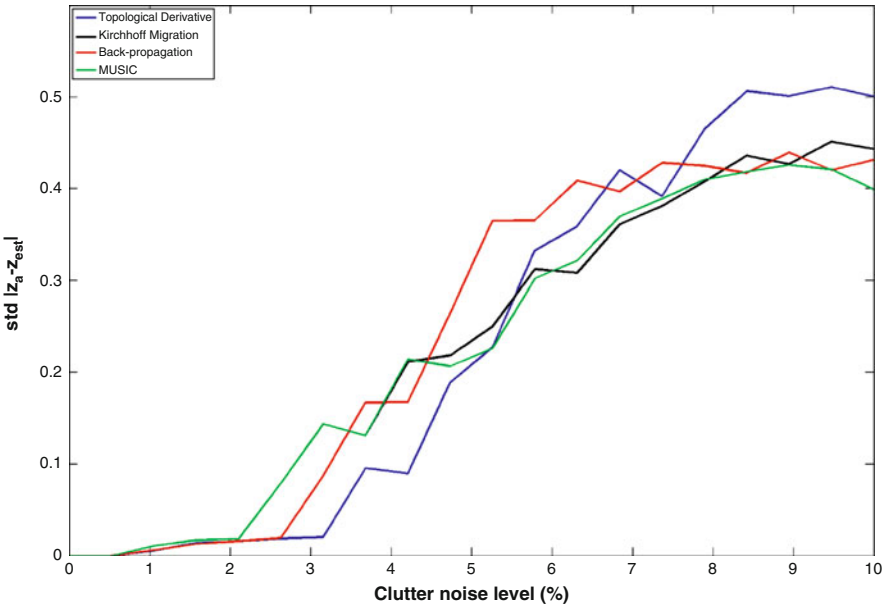

Fig. 2.11. Standard deviations of the localization error with respect to clutter noise for $\mathcal{I}_{\mathrm{MU}}, \mathcal{I}_{\mathrm{BP}}, \mathcal{I}_{\mathrm{KM}}$, and $\mathcal{I}_{\mathrm{TD}}$ with $n = 50$

Measurement Noise

We solve the Helmholtz equation for the n illuminations and m frequencies. We then add a white Gaussian noise with standard deviation σ ranging from 0 to 120% of the L^2 norm of the measurements. We apply the algorithms (Kirchhoff Migration MF, Matched Field MF and Topological Derivative TDF) and plot as previously the standard deviation of the localization error $|\boldsymbol{z}_{\mathrm{est}} - \boldsymbol{z}_a|$ as of function of the noise level for $N_r = 250$ realizations.

Figure 2.12 shows the robustness of $\mathcal{I}_{\mathrm{TDF}}$. We also see from Fig. 2.12 that the multifrequency approach yields an improvement by a factor of $\sqrt{m}$ in the SNR. Here the noise acts incoherently on the amplitude of the signal but not on its phase. Averaging multifrequency measurements cancels such incoherent noise. Moreover, given the expression (2.20) of the SNR of Kirchhoff Migration as a function of ω, it is expected that we should observe even slightly better stability if we repeat m experiments at the highest available frequency available and use $\mathcal{I}_{\mathrm{KMF}}$ for image reconstruction.

Medium Noise

We simulate a clutter as described previously with σ still ranging from 0 to 10% of the mean value of the process μ. Here, measurements at each frequency

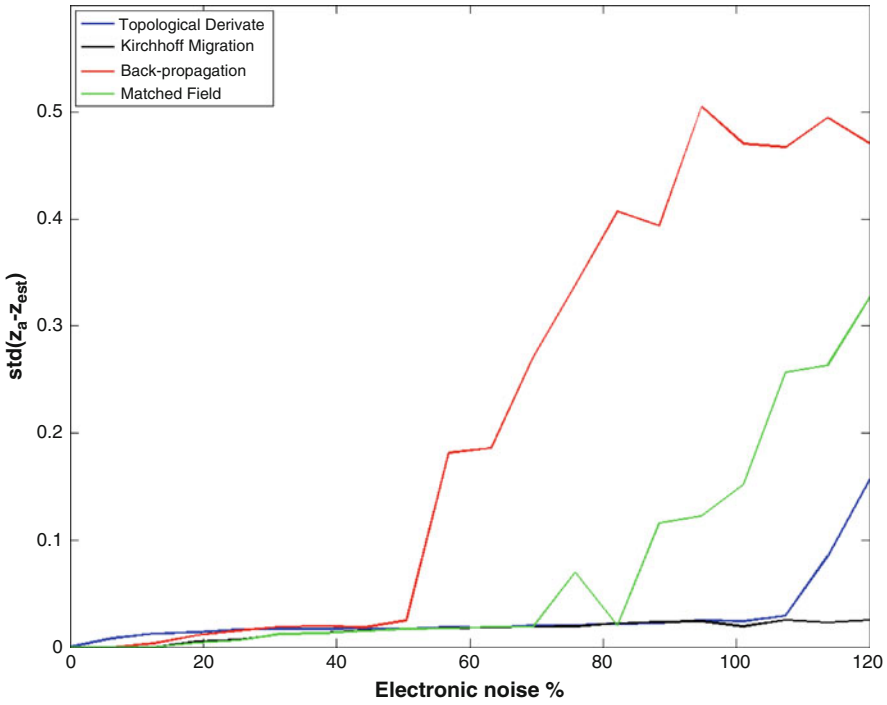

Fig. 2.12. Standard deviations of the localization error with respect to measurement noise for $\mathcal{I}_{\mathrm{BPF}}, \mathcal{I}_{\mathrm{KMF}}, \mathcal{I}_{\mathrm{MF}}$, and $\mathcal{I}_{\mathrm{TDF}}$ with $m = 30$ and $n = 50$

will be obtained in the same noisy medium. We cannot observe noise cancellation because the noise induced by such clutter is coherent and acts on the phase of the signal. Indeed, taking multifrequency measurements and bluntly summing is not what should be done. Given the SNR of $\mathcal{I}_{\mathrm{TD}}$ in this case [3], we can compute the frequency for which we will get the most stable image. It is the frequency at which the SNR is maximal:

$$\omega_{\mathrm{best}} = \frac{2}{\sigma}\sqrt{\frac{2}{l_\mu L_\mu}},$$

where l_μ is the correlation length of μ and L_μ is the propagation distance through the clutter. Since in our case l_μ and σ are small and L_μ is of order one, ω_{best} is out of the chosen frequency range. Our best shot is then to use $\omega = \omega_{\max}$.

Figure 2.13 illustrates the previous observation: summing over frequencies the topological derivative imaging functional seems to be counter-productive for a clutter noise medium. A solution to make use of multifrequency measurements in the case of noisy medium could be the CINT inspired approach described previously. However, the computations become really

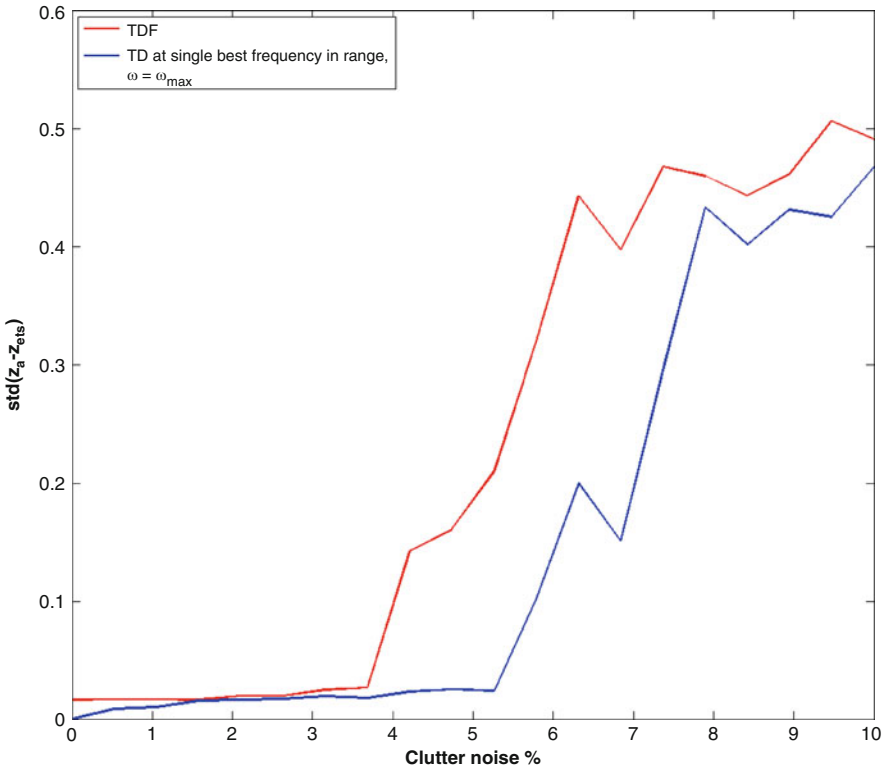

Fig. 2.13. Standard deviations of the localization error with respect to medium noise for $\mathcal{I}_{\text{TDF}}$ with $m = 30$ and $n = 50$ and $\mathcal{I}_{\text{TD}}$ at $\omega_{\max}$ for $n = 50$

heavy and tuning of the parameters Ω_D, X_D really fine, preventing a large scale stability analysis as the one we carried out for other direct algorithms.

2.5 Conclusion

In this chapter we have compared the performance of direct anomaly detection functionals at a fixed as well as multiple frequencies. We have carried out a numerical stability and resolution analysis in the presence of medium and measurement noises. In the case of multifrequency measurements, we have proposed a CINT-type imaging functional to correct the effect of an unknown cluttered bulk modulus (random fluctuations around a known constant) on anomaly detection. We have proved that the topological derivative imaging functional is quite robust with respect to both measurement and medium noises.

Acknowledgments

This work was supported by the ERC Advanced Grant Project MULTIMOD–267184.

References

1. H. Ammari, An Introduction to Mathematics of Emerging Biomedical Imaging, Mathematics & Applications, Vol. 62, Springer, Berlin (2008)
2. H. Ammari, E. Bretin, J. Garnier, V. Jugnon, Coherent interferometry algorithms for photoacoustic imaging, SIAM J. Numer. Anal., to appear.
3. H. Ammari, J. Garnier, V. Jugnon, H. Kang, Stability and resolution analysis for a topological derivative based imaging functional, SIAM J. Control Opt., to appear.
4. H. Ammari, J. Garnier, H. Kang, W.-K. Park, K. Sølna, Imaging schemes for perfectly conducting cracks, SIAM J. Appl. Math. **71**, 68–91 (2011)
5. H. Ammari, J. Garnier, K. Sølna, A statistical approach to target detection and localization in the presence of noise, Waves in Random and Complex Media, to appear.
6. H. Ammari, E. Iakovleva, D. Lesselier, A MUSIC algorithm for locating small inclusions buried in a half-space from the scattering amplitude at a fixed frequency, Multiscale Model. Simul. **3**, 597–628 (2005)
7. H. Ammari, H. Kang, Reconstruction of Small Inhomogeneities from Boundary Measurements, Lecture Notes in Mathematics, Vol. 1846, Springer, Berlin (2004)
8. H. Ammari, H. Kang, Polarization and Moment Tensors: with Applications to Inverse Problems and Effective Medium Theory, Applied Mathematical Sciences, Vol. 162, Springer, New York (2007)
9. H. Ammari, H. Kang, Expansion Methods, *Handbook of Mathematical Methods in Imaging*, 447–499, Springer, New York (2011)
10. H. Ammari, H. Kang, H. Lee, Layer Potential Techniques in Spectral Analysis, Mathematical Surveys and Monographs, Vol. 153, American Mathematical Society, Providence RI (2009)
11. N. Bleistein, J.K. Cohen, J.W. Stockwell Jr., *Mathematics of Multidimensional Seismic Imaging, Migration, and Inversion*, Springer, New York (2001)
12. M. Bonnet, B.B. Guzina, Sounding of finite solid bodies by way of topological derivative, Int. J. Numer. Meth. Eng. **61**, 2344–2373 (2004)
13. L. Borcea, G. Papanicolaou, C. Tsogka, Theory and applications of time reversal and interferometric imaging, Inverse Probl. **19**, 134–164 (2003)
14. L. Borcea, G. Papanicolaou, C. Tsogka, Interferometric array imaging in clutter, Inverse Prob. **21**, 1419–1460 (2005)
15. M. Brühl, M. Hanke, M.S. Vogelius, A direct impedance tomography algorithm for locating small inhomogeneities, Numer. Math. **93**, 635–654 (2003)
16. J. Garnier, Use of random matrix theory for target detection, localization, and reconstruction, Contemporary Math., **548**, 1–20, Amer. Math. Soc., (2011)
17. L. Klimes, Correlation functions of random media, Pure Appl. Geophys. **159**, 1811–1831 (2002)
18. G.W. Milton, The Theory of Composites, Cambridge Monographs on Applied and Computational Mathematics, Cambridge University Press (2001)

19. M.S. Vogelius, D. Volkov, Asymptotic formulas for perturbations in the electromagnetic fields due to the presence of inhomogeneities, Math. Model. Numer. Anal. **34**, 723–748 (2000)
20. D. Volkov, Numerical methods for locating small dielectric inhomogeneities, Wave Motion **38**, 189–206 (2003)

Springer

http://www.springer.com/978-3-642-22989-3

Mathematical Modeling in Biomedical Imaging II
Optical, Ultrasound, and Opto-Acoustic Tomographies
Ammari, H. (Ed.)

2012, IX, 160 p. 43 illus., 38 illus. in color., Softcover
ISBN: 978-3-642-22989-3